Submitted to CIRP6: 6th International Conference on Infrared Lasers, Ascona, Zurich, Switzerland, May 29-June 3, 1994.

Conf-9405172--1

BNL-60452

PICOSECOND CO_2 LASER FOR RELATIVISTIC PARTICLE ACCELERATION *

I. Pogorelsky, I. Ben-Zvi
Brookhaven National Laboratory
Upton, NY 11973, USA

W.D. Kimura
STI Optronics
Bellevue, WA 98004, USA

N.A. Kurnit
Los Alamos National Laboratory
Los Alamos, NM 87545, USA

F. Kannari
Keio University
Yokohama, Japan

Abstract

A table-top 20-GW 50-ps CO_2 laser system is under operation at the Brookhaven Accelerator Test Facility. We compare laser performance with model predictions. Extrapolations suggest the possibility of compact terawatt CO_2 laser systems suitable as laser accelerator drivers and for other strong-field applications. Latest progress on an Inverse Cherenkov Laser Accelerator experiment is reported.

I. INTRODUCTION

The continued interest in high-peak-power molecular gas laser development is based on the ability to build fairly economical high-aperture, large-volume generators and amplifiers with high energy output and high repetititon rates. CO_2 lasers are the most prominent representative of this class of lasers for the IR spectral region. The list of traditional scientific applications of pulsed CO_2 lasers includes: plasma physics, laser chemistry, molecular spectroscopy, far-IR laser pumping, the study of nonlinear effects in semiconductors, and lidars.

Laser-driven particle accelerators is another emerging area for high-power lasers that like many other applications may benefit from long-wavelength CO_2 laser radiation delivered in short picosecond pulses. However, because of the relatively narrow rotational structure typical for molecular gas spectra ($\approx 10^{10}$ Hz), picosecond pulse formation via a mode-locking technique has not been as successfully obtained with CO_2 lasers as with solid state lasers, which have wide crystal-host broadening of the individual ion spectral lines ($10^{11} - 10^{12}$ Hz). That is why alternative ways to produce CO_2 pulses with picosecond time scales have been developed including: optical free-induction decay (OFID),[1] optical parametric oscillation,[2] and semiconductor switching.[3,4]

With semiconductor switching and consecutive regenerative amplification, up to 1.5 GW 2-ps CO_2 laser pulses were produced in a 1-mm^2 beam.[5] However, the potential for high-peak-power extraction in a single picosecond pulse from a high-volume gas amplifier has not been capitalized so far.

In the present paper we report on a multi-gigawatt CO_2 laser system based upon single picosecond pulse generation and multi-pass amplification. The system is now operational at

*This work done under the auspices of the U.S. Department of Energy.

MASTER

DISTRIBUTION OF THIS DOCUMENT IS UNLIMITED

the Brookhaven Accelerator Test Facility[6] (ATF) to test several laser acceleration schemes[7,8,9] in which a high-power CO_2 laser beam interacts with a 50 MeV e-beam produced by an RF linac.

The basic physical principles of the picosecond pulse generation and amplification are outlined in Section II.

In Section III, we present the design and performance of the ATF CO_2 laser system.

The application of the ATF CO_2 laser system as a driver for an inverse Cherenkov laser accelerator is described in Section IV.

In Section V, we consider the potentials to scale-up the CO_2 laser system into the terawatt power region and its advanced application within the ATF Laser Accelerator Test Program.

Conclusions are oulined in Section VI.

II. PRINCIPLES OF PICOSECOND 10-μm PULSE GENERATION AND AMPLIFICATION

II.1. Semiconductor Switching of Picosecond Pulses

The picosecond switching method used in the ATF CO_2 laser system is based on modulating the reflective and transmissive properties of a semiconductor by optically controlling the free-carrier charge density. A short-wavelength picosecond laser pulse with a photon energy above the band gap of the semiconductor creates a highly reflective electron-hole plasma in the surface layer of the semiconductor, such as germanium, which is normally transparent to 10-μm radiation. The free-electron density, N_e, at the semiconductor surface is linearly proportional to the absorbed control-pulse fluence E per unit area by the relation

$$N_e = \alpha E/(h\nu), \tag{1}$$

where α is the absorption coefficient and $h\nu$ is the photon energy. For a Nd:YAG control laser, α^{-1}=1 μm, and, for a characteristic pulse fluence of $E \approx 2$ mJ/cm^2, the density of excess free carriers, N_e, created in Ge is more than 2×10^{19}/cm^3, which is just above the critical electron density $N_{cr} = 1.6 \times 10^{19}/cm^3$ given by

$$N_{cr} = \omega^2 m_e n_0^2/4\pi e^2, \tag{2}$$

where ω is the radiation frequency, m_e the electron mass, and n_0 the refractive index at normal conditions. The refractive index drops due to free carriers according to the equation:

$$n = n_0 (1 - N_e/N_{cr})^{1/2}. \tag{3}$$

n turns imaginary at $N_e > N_{cr}$ and a semiconductor slab switches from a window at 10μm to a highly reflective mirror due to its "metallization" by the picosecond control pulse.

After termination of the control pulse, the main process governing the time evolution of the excess free carriers at the surface, and hence the reflectivity, will be ambipolar diffusion:[3]

$$N_e(t) = N_e(0) \exp(\alpha^2 Dt)\, \mathrm{erfc}\left[\alpha (Dt)^{1/2}\right], \tag{4}$$

where the ambipolar diffusion constant $D = 65$ cm^{2}sec^{-1}, and $N_e(0)$ is the free-carrier density at the end of the control pulse according to Eq.(1). The characteristic time, $\alpha^{-2}D^{-1}$, is then 150 ps. Electron-hole recombination is much slower with a typical time of $\approx$ 50 ns.[4]

To define the trailing edge of the pulse, shortening it to a few picoseconds, the complement to reflection switching, transmission switching, may be used for a second stage. An optically

delayed control pulse cuts off the trailing edge of the transient pulse by initiating reflection and absorption with a $\sigma = 6 \times 10^{-16}$ cm^2 cross-section.[10] Absorption makes the Ge slab opaque for 10μm radiation during the time while the electron-hole recombination takes place. The resulting "sliced" transmitted pulse has the desired few-picosecond length determined by optical delay adjustment of the control radiation before the transmission switch.

II.2. Bandwidth Limitations in Amplification of the Picosecond CO_2 Laser Pulses

When a short laser pulse propagates in a resonant-amplifying molecular medium, two characteristic spectral parameters and their corresponding time constants should be taken into consideration. The first is a time, δt, corresponding to the frequency interval between the centers of the V-R lines, which is 18 ps for the P-branch of the 10-μm band. The other is the collisionally induced dipole dephasing time, T_2, related to a Lorenzian line shape of a V-R transition by

$$T_2 = (\pi \delta \nu)^{-1},$$

where the FWHM $\delta\nu$ is inversely proportional to the gas pressure. For a 1 atm CO_2-laser gas mixture, $T_2 \approx 100$ ps.

The behavior of picosecond CO_2 pulse amplification was analyzed by a numerical solution of the Maxwell-Bloch equations. Let us consider how the character of amplification of the CO_2 laser pulse depends upon the relative magnitude between the initial duration τ_0, and time constants δt and T_2.

a) $\tau_0 < \delta t < T_2$:

The spectral width of a short laser pulse (less than 18 ps) may cover several discrete transition lines. The electric field of such an input pulse excites a polarization in CO_2 molecules, which are in various rotation states. Since molecules in different states are characterized by different frequencies, these polarization components eventually become dephased. As a result, the spectral and time structure of the induced radiation will not remain equal to those of the initial pulse. At a low, $\approx$1 atm, gas pressure the discrete gain spectrum transforms the spectrum of the input pulse from continuous to discrete, and its Fourier transform corresponds to a pulse train with a δt period. Even at 10 atm pressure, when the broadening effect partially smooths the discrete gain spectrum, the pulse splitting is still noticeable (see Fig.1(a,b)). An alternative to achieve gain smoothing is reducing the spectrum modulation period by using an isotopic gas mixture. Replacement of one of the oxygen nuclei by that of a different isotope destroys the symmetry of the CO_2 molecule. That means that twice as many V-R transitions are allowed and the gain spectrum becomes twice as dense as with a regular CO_2 molecule. If we consider a mixture $^{12}C^{16}O_2$:^{12} $C^{16}O^{18}O$:^{12} $C^{18}O_2$ = 1:2:1, then, due to isotopic shifts, the combined spectrum will have in overlaped regions approximately 4-times denser rotational structure than with a regular CO_2 molecule. Computer modeling shows that the reduction in the spectral line interval results in considerably less short-pulse distortion during amplification (see Fig.1(c)).

b) $\delta t < \tau_0 < T_2$:

If the input laser pulse width, τ_0, is longer than δt, then just one rotational line is involved in the amplification. During the amplification, the spectrum of the input pulse is filtered by the gain spectrum and eventually the pulse duration increases according to the relation:[11]

$$\tau(l) \approx \tau_0 \left[1 + 4ln2\,(T_2/\tau_0)^2\, g_o l \right]^{1/2}. \qquad (5)$$

This effect is illustrated by computer modeling results in Fig.1(d,e). Pulse broadening is most pronounced at atmospheric or lower pressure, when the spectral width of the individual V-R

transition is much less than the spectral separation between the rotational lines, and the gain spectrum may be considered as discrete.

c) $\tau_0 >> T_2$:

Pressure broadening of the individual rotational lines helps to minimize the pulse shape distortion. Because T_2 is inversely proportional to the gas pressure, it becomes $\approx$10 ps at 10 atm. Numerical calculations demonstrate that pulses longer than 20 ps can propagate without appreciable distortions. Fig.1(f) gives the illustration for τ_0=30 ps pulse amplification.

In general, if τ_0 is much longer than T_2 (in other words, the spectrum of the input pulse is narrower than the individual V-R line), the pulse can propagate without distortion up to a certain energy level at which a saturation effect shortens the pulse width. The saturation energy level depends upon the pulse length and molecular relaxation time constants. A CO_2 laser has two kinds of saturation energy:

$$E_S^0 = \frac{h\nu}{2\sigma}, \quad and \quad E_S = \frac{E_S^0}{Z[j_{max}]},$$

where $Z[j_{max}]$ is the maximum relative population of the rotational level in the upper laser vibrational state. These quantities correspond, respectively, to the single rotational line saturation energy and to saturation of all rotational lines, i.e. the total vibrational level. If τ_0 is much longer than the characteristic time constant for rotational relaxation, τ_R, the amplification process is governed by the vibrational level saturation energy, E_S. Note, that τ_R is inversely proportional to gas pressure and at 3 atm is equal to 50 ps. For a Boltzman thermal distribution in the discharge, $Z[j_{max}] = 0.065$, and using a value of $\sigma = 5\times10^{-19}$ cm^2 for the 10P(20) line, we obtain $E_S = 350$ mJ/cm^2.

In the situation when τ_0 becomes comparable with τ_R, it is difficult to estimate the effective E_S^* value without a computational analysis. E_S^* may be obtained in this case as the best fit to the Franz-Nodvik function

$$E_{out} = E_S^* \; ln[\; 1 + exp(g_o l)[exp(E_{in}/E_S^*) - 1\;]\;]. \qquad (6)$$

III. DESIGN AND PERFORMANCE OF THE ATF CO_2 LASER SYSTEM

III.1. *Semiconductor Slicer*

The schematic of the optical set up used in the experiment is presented in Fig.2. The hybrid single-longitudinal zero-transverse mode TEA CO_2 laser oscillator is the source of the 10-μm beam. The control beam for the CO_2 oscillator pulse slicing by means of semiconductor switches is provided by a picosecond Nd:YAG laser system. The output 20-mJ Nd:YAG pulse is frequency quadrupled to drive the photocathode of the ATF linac's electron gun. The unconverted infrared is sent to the switching system. The use of the same Nd:YAG pulse to control both the linac and the CO_2 slicing system ensures an adequate synchronization of the e-beam and CO_2 laser pulse on the picosecond time scale necessary for the ATF laser accelerator experiments.

Intrinsic Ge slabs are used for the semiconductor switches. Generated by the CO_2 oscillator, the p-polarized laser beam illuminates the Ge slab at the Brewster angle 76° to ensure a low background reflection that does not exceed 3×10^{-6}. Up to 100% of the incident CO_2 oscillator peak power is reflected when $\approx$5 mJ of the control energy is absorbed on the first Ge switch. After a variable time-delay introduced by a prism, the residual Nd:YAG energy, not absorbed on the reflection switch, is directed to the second Ge switch, onto the spot irradiated by the transient CO_2 pulse. It truncates the CO_2 tail by means of both plasma reflection

and absorption. The CO_2 laser peak power after slicing is ≈0.5 MW with a contrast ratio of 10,000:1.

Using the 20-ps Nd:YAG control pulse, the sliced pulse duration is variable between 30-300 ps. Keeping in mind the spectral-band restrictions to sustain short picosecond pulses (see Section II.2), this pulse duration is adequate for the present ATF 3-atm CO_2 amplifier.

III.2. Multipass Amplification

A 3-atm multipass CO_2 amplifier pumped by a UV-preionized transverse electric discharge serves to increase the peak power of the sliced 10 μm pulse from 0.5 MW up to the ≈10-GW level required for the laser acceleration experiments. The laser amplifier head consists of a cylindrical plexiglas vessel designed to house the main discharge electrodes and the preionizing spark-gap arrays. Two sets of serially-placed brass electrodes define the discharge volume of 2x5x60 cm^3 (x2) = 1,200 cm^3. Preionization spark-gap arrays are arranged in series along the side walls of the discharge volume and a sliding spark is excited by a 35 kV voltage pulse. The amplifier cell rests on an oil tank containing the high-voltage pulse-forming circuit. Two sets of 2-stage Marx generators supply up to 140 kV pulses to the main discharge with a specific energy loading of up to 650 J/l.

The requirements of arc-free and mechanically safe operation of the amplifier discharge cell place a 3-4 atm limit on the working gas pressure. Gas mixture composed of CO_2:N_2:He in proportion 1:0.5:8.5 was normally used. Small signal gain (SSG) up to 2.4 % /cm at 10.6 μm was measured under these conditions.

The 8-pass optical configuration chosen to amplify the sliced picosecond CO_2 laser pulse up to a multi-gigawatt level is presented by Fig.3. Four passes are arranged using a set of four mirrors placed on both sides of the amplifier cell. Due to the limited aperture of the amplifier cell, no additional mirrors may be placed without creation of a quasi-stable cavity that causes self-lasing build-up. Consequently, the same 4-mirror set is used for additional 4 passes. To suppress parasitic feedback through the optical path while redirecting the beam for the next 4 passes, an optical polarization isolator is placed in the way of the amplified beam.

The optical isolator consists of a polarizer (Ge Brewster plate) with a Pockels cell in front of it. The polarizer is set in a crossed orientation to the ZnSe Brewster windows of the amplifier. By applying a 10-ns 8-kV pulse to the electro-optically birefringent CdTe crystal of the Pockels cell synchronously with the picosecond pulse arrival, we turn the pulse polarization 90° in order to transmit the pulse through the polarizer. A telescope is placed in front of the Pockels cell to properly shape the beam diameter and divergence. It performs another important function as well, shortening the amplified laser pulse by means of optical self-breakdown in a pinhole placed at the focal point.

Fig.4 shows the energy evolution when various duration laser pulses are amplified.

The duration of the laser pulse after self-breakdown is regulated by the time required for the optical breakdown development and does not depend much upon the initial duration of the sliced pulse. That is why all experimental energy curves in Fig.4 terminate after 8 passes through the amplifier at about the same final output energy of ≈1 J.

Presented in Fig.5 are autocorrelation curves recorded with a single-shot autocorrelator that illustrate the observed effect of pulse shortening due to optical self-breakdown.

Deconvolution of the autocorrelation curve in Fig.5(b) gives an estimate of 40-ps FWHM Gaussian pulse duration corresponding to ≈25 GW peak power attained in 8 passes.

IV. ELECTRON ACCELERATION WITH PICOSECOND CO_2 LASER

IV.1. Overview of Methods

Laser-driven particle accelerators is a newly emerging application area for high-power lasers. The fundamental motivation for studying laser-driven particle accelerators is the ultra-high fields attainable with high-intensity pulsed lasers. For instance, the transverse electric field corresponding to an intensity of 10^{16} W/cm^2 is more than 300 GV/m. Various laser acceleration concepts involve transforming a fraction of this enormous field into an effective accelerating field.[7-9,12,13] Several of them[7-9] will be tested at the ATF using the picosecond CO_2 laser described in the previous sections and the 50-MeV electron linac.

In general, particle acceleration with a fast-oscillating field becomes possible if phase synchronism of the driving field with a particle bunch over the acceleration length is satisfied. The relatively long wavelength of a CO_2 laser helps to meet this requirement. This is illustrated by the ATF laser accelerator schemes.

One of them, called the Grating Linac[9], is based on excitation of a surface standing wave field when a laser beam is cylindrically focused onto a periodic structure. Electrons injected along the surface will be accelerated when moving in phase with the field oscillation. This happens when

$$L_G = \beta\lambda_l,$$

where L_G is the period of the grating, λ_l is the laser wavelength, and $\beta = v/c$ is the normalized electron speed. For relativistic electrons, the period of the grating should be nearly equal to the laser wavelength, $L_G \approx \lambda_l$. We see that relatively long CO_2 laser wavelength helps to build reasonably macroscopic structures. 1 GV/m acceleration is predicted in this scheme with a cylindrically focused CO_2 laser beam of 700 GW/cm^2 intensity.

The Inverse Free Electron Laser Accelerator is based on the accelerating action of a linearly polarized laser beam on electrons having an oscillating trajectory inside a wiggler. The synchronism condition for a planar wiggler is[7]

$$\lambda_l = 2.2 \times 10^3 \lambda_w^3 B_w^2/\gamma^2, \tag{7}$$

where λ_w(m) is the wiggler period, B_w(T) is the wiggler magnetic field, and γ is the relativistic factor. This condition may be satisfied by adjusting the wiggler field and period. Model simulations predict 100 MV/m acceleration with a 200 GW CO_2 laser beam interacting with electrons in a properly tapered wiggler.

In the Inverse Cherenkov Accelerator (ICA), the phase matching condition is satisfied when a laser beam intersects the e-beam at the Cherenkov angle, θ_c, in a medium with the refractive index n. That is:

$$cos\theta_c = 1/(n\beta). \tag{8}$$

Hydrogen gas is used as the phase-matching medium due to its low electron scattering characteristics. Because of the wave-front inclination, a longitudinal component of the electric field is developed. The long CO_2 laser wavelength means that acceleration process is less sensitive to dephasing phenomena, such as gas scattering or the electron and light velocities mismatch during the acceleration.

IV.2. Design of ICA Experiment at ATF

The geometry of the ATF ICA experiment was proposed by Fontana and Pantell.[13] In their scheme, the efficiency of the laser light coupling to the e-beam is increased when a radially polarized laser beam is focused along the e-beam direction by an axicon, as schematically

demonstrated in Fig.6. Monte Carlo computer simulation predicts up to 38 MeV net acceleration for θ_c=20 mrad, L=20 cm, H_2 pressure of 1.7 atm, and laser intensity of I=50 GW.

A plan view of the actual design of the accelerator chamber is presented in Fig.7. A filament e-beam of $\approx$500 μm diameter, enters and exits the hydrogen-filled chamber through diamond film windows made 2 μm thick to prevent electron scattering. The laser beam enters the cell through a ZnSe window and reflects off a 45° flat mirror to the axicon mirror. The axicon has 0.5 mm diameter central hole drilled for the e-beam to travel through. The axicon is cut with a 10 mrad apex angle, which results in a Cherenkov angle of θ=20 mrad. The laser beam reflects off the axicon and is focused down onto the e-beam. After interacting with the e-beam, the spent laser beam reflects off the 45° mirror and exits the chamber. The spent beam can then be further analyzed using optical detectors located outside the chamber.

IV.3. Radial Polarization Conversion

The ATF ICA experiment is based on using a radially polarized laser beam. The polarization converter is placed between the linearly polarized CO_2 amplifier output and accelerator chamber. The double interferometer optical set-up used as the radial polarization converter is presented in Fig.8.[14] Key elements of the converter are two spiral phase delay (SPD) plates placed in two legs of the first interferometer stage. The optical thickness increment of the SPD plate at 2π azimuth rotation is equal to one wavelength for CO_2 light. Oriented in opposite directions, two SPD plates produce clockwise and counter-clockwise spiral wavefronts from the original plane-wave laser beams. The combination of these two counter-rotating wave fields on a 50%-beamsplitter after the first interferometer stage produce a stationary two-lobe angular distribution, in analogy with a stroboscopic effect in mechanics. Actually, the laser beams propagating in the two legs of the second interferometer stage have orthogonally oriented intensity distributions. This is the result of a π phase shift via the reflection at the 50%-beamsplitter at the air/coating surface and a zero-shift due to reflection at the ZnSe/coating surface. After introducing a 90° polarization rotation by a conventional $\lambda/2$ retardation plate placed in one leg of the second interferometer, the resulting orthogonally oriented and orthogonally polarized distributions are combined at a polarizing beamsplitter as illustrated by Fig.9. As a result, a radially polarized beam is produced in agreement with the mathematical formalism developed for this type of polarization converter.[14]

IV.4. Axicon Focusing

When a radially polarized beam is focused by the axicon a circularly symmetric interference pattern is developed along the optical axis of the axicon. Assuming a uniform intensity distribution in the input laser beam, the analytical solution for the longitudinal component of the electric field $E_z(r)$ is a Bessel function of the first order:[13]

$$E_z(r) = E_0 \times J_0(kr\theta_c/\beta) \tag{9}$$

with

$$E_o = 2\left(\frac{\pi P}{\lambda_l L}\right)^{1/2}\left(\frac{\mu_0}{\epsilon_0}\right)^{1/4} sin\theta_c,$$

where P(Watt) is the laser power, and L(m) is the interaction length according to Fig.6. The e-beam used in the acceleration experiment has a radius less than the radial position of the first minimum in the distribution Eq.(9)

$$r_{min} = 0.38\lambda/\theta_c$$

and r_{min}=0.20 mm for θ_c=20 mrad. Assuming no phase slippage of electrons, we have the equation for net acceleration:

$$\Delta W = eE_0 L cos\psi, \tag{10}$$

where e is the electron charge, ψ is the phase of the longitudinal electric field seen by the electron. Under the conditions of the ATF ICA experiment, with the input laser beam diameter d=10 mm and L=20 cm we get

$$\Delta W = 0.26\sqrt{P} cos\psi, \tag{11}$$

where ΔW is measured in keV. More accurate Monte Carlo numerical simulations[15] take into the account the phase slippage during the acceleration due to the effects of gas scattering and the actual laser beam distribution at the axicon. However, the square root dependance of the maximum acceleration upon the laser peak power is still preserved.

IV.5. ICA Laser Acceleration Test

In a recent ICA experiment, 0.7 GW peak laser power was delivered to the interaction region. Figures 10(a) and 10(b) show the electron beam energy spectrum, both Monte Carlo simulations and data, with the laser off or on, respectively. The observed widening of the spectrum with the laser present is because the electrons are uniformly distributed over the laser wave phase resulting in both accelerated and decelerated electrons. The detector sensitivity limited observing the highest accelerated electrons in Fig.10(b). With the detector set to maximum gain, up to 3.7 MeV acceleration was actually measured in reasonable agreement with theory. Upon the improvement of the electron detector and optical transport system, the ICA experiment will be run with up to 10 GW peak laser power for which 12 MeV maximum electron acceleration is expected.[15]

V. APPROACH TO COMPACT TERAWATT CO_2 LASER SYSTEM

The next milestone in the laser accelerator development would be a ΔW=100 MeV experimental demonstration and, based on it, a 1 GeV laser accelerator design. The ATF laser accelerator schemes are potentially scalable to ΔW=100 MeV.[7,10] The proposal for a 100 MeV Inverse Cherenkov Accelerator[16] would use the existing accelerator section as an electron buncher. After passing this stage, electrons will be bunched along the axis of propagation with the interval equal to the laser wavelength. Using the bunched e-beam improves the acceleration efficiency through better phasing of the electrons with the accelerating laser field. Computer simulations made for a 3-stage accelerator with 50 GW of laser peak power delivered to each 20-cm long stage shows that electrons with an initial energy of 50-MeV will be accelerated to 150 MeV.[16]

Let us consider the possibilities and principal limitations for further scale-up of a single-beam picosecond CO_2 laser system to meet the requirements of advanced laser accelerators. To be more specific, a TE laser module with a 10-cm aperture size and up to 10 atm pressure will be considered as a second amplifier. Such devices are feasible with x-ray or e-beam preionization of the discharge volume.

Starting from the presently demonstrated $I \approx 10$ GW/cm^2 flux at the ATF amplifier output and using Maxwell-Bloch modeling we predict 150 GW output from a large-aperture 3-pass 3-atm second amplifier, presuming its specific characteristics are similar to those of the present ATF amplifier.

The increase of the amplifier pressure from 3 atm to 5 atm results in E_S^* increasing from 50 mJ/cm^2 to 100 mJ/cm^2 via σ and τ_R drop. Some reduction of the initial pulse duration is also possible when the amplifier pressure is increased. Due to all these factors, up to 300 GW peak power is expected out of a 5-atm large-aperture second amplifier.

A 10-atm x-ray or e-beam preionized CO_2 discharge module is still a better candidate for a final amplifier, providing the prospect for even higher peak power via a combination of the increased energy and pulse shortening. Under higher energy loading ($\approx$1.5 kJ/l) attainable with such devices and because of optimization of the normalized electric field (E/P) with more powerfull external ionization, the specific energy storage at the upper vibrational CO_2 (001) laser level increases $\approx$8 times, reaching a value of 120 J/l, in comparison with 15 J/l for the 3-atm UV-preionized discharge. Faster rotational relaxation, $\tau_R \approx$20 ps, and higher saturation fluence, $E_S^* \approx$500 mJ/cm^2, complete the argument in favor of the energetic feasibility to extract up to I=100 GW/cm^2 flux from the 10-atm amplifier in a 50-ps pulse.

However, the practical limitations to the intensity increase in picosecond CO_2 laser beams will be set by the optical component (windows, mirrors) damage and gas breakdown. Analyzing the experimental data available on gas breakdown and optical material damage with picosecond CO_2 laser pulses, we come to two conclusions:

a) Both effects are described by an electron avalanche multiplication mechanism (at I <1 TW/cm^2). This mechanism assumes inverse proportionality between the breakdown threshold flux, I_{th}, and laser pulse duration, τ, $I_{th} \sim \tau^{-1}$, or the invariance of the threshold fluence, E_{th}, with τ.

b) Optical window damage is the major limitation in energy scaling of picosecond CO_2 lasers. However, laser pulse shortening should provide a nearly proportional increase of the flux that may be transmitted through the window without its damage. For example, E_{th}=0.5 J/cm^2 was measured for a NaCl window with 2-ps CO_2 laser pulses,[5] that is equivalent to I_{th}=0.25 TW/cm^2.

In order to amplify pulses as short as a few picoseconds, a multi-isotope laser gas mixture, e.g. $^{12}C^{16}O_2$:^{12} $C^{16}O^{18}O$:^{12} $C^{18}O_2$ = 1:2:1, may be used. According to the computer simulations, as short as 3 ps pulses may be amplified without significant distortions in a 5-atm multi-isotope discharge. The bandwidth of a 3-ps pulse covers the whole 10P CO_2 branch resulting in efficient energy extraction from the (001) vibrational level. However, this smoothing of the spectrum also results in $\approx$2 times drop of the small signal gain in comparison with a regular mixture at the same pressure. Because of the considerably lower gain, two multipass amplifier stages are not enough to approach the optical-damage-limited output power. Instead of using an extra stage, we consider another option presented in Fig.11: a single-pulse regenerative preamplifier. We expect that its output will be limited to $\approx$10 GW (for a 3-ps pulse) by the Pockels cell optical damage. Additional two passes through the same discharge cell will follow bringing the power to $\approx$100 GW. Due to the high saturation energy, $E_S^* \approx$600 mJ/cm^2, computed for a multi-isotopic mixture, the second amplifier will increase the peak power to the $\approx$3 TW level in a nearly linear regime.

VI. CONCLUSIONS

A compact table-top 20-GW 50-ps CO_2 laser system has been build and is available now for strong field physics study at the ATF, BNL. As high as 40,000 power gain has been demonstrated in a single amplifier stage used in a multipass scheme with internal active feedback isolation. A simple plasma shutter used in combination with a semiconductor switching technique helps to improve performance of the system via pulse shortening and suppression of parasitic oscillation in the amplifier.

For various applications, a high-power picosecond CO_2 laser presents certain advantages over more commonly known nanosecond CO_2 laser systems of comparable peak power. For instance, problems of optical damage and breakdown will be less severe than for nanosecond lasers of the same power. One such ongoing applications is laser-driven particle acceleration. Several laser accelerator schemes benefit from the relatively long wavelength of CO_2 lasers that helps particles to stay longer in phase with the accelerating electromagnetic wave.

Such laser accelerator concepts are under test at the ATF where 20-GW 50-ps CO_2 laser pulses are brought into the interaction with 50-MeV 10-ps electron bunches. Preliminary results on electron acceleration to several MeV using the Inverse Cherenkov Laser Accelerator scheme promise further progress of this research to the next milestone of 100 MeV laser acceleration. The proposed upgrade of the picosecond CO_2 laser to the terawatt peak power level meets the requirements for the advanced laser accelerators.

ACKNOWLEDGMENT

This work was supported by the Department of Energy, Contract No. DE-ACO2-76CH00016 and No. DE-AC06-83ER40128.

REFERENCES

1. E. Yablonovich and J. Goldar, *Appl. Phys. Lett.*, **25**, 580 (1974); R.Kesselring, A.W. Kahlin, H.J. Schotzau, and F.K. Kneubuhl, *IEEE J. Quant. Electron.*, **29**, 997 (1993).

2. A. Laubereau, L. Greiter, W. Kaiser, *Appl. Phys. Lett.*, **25**, 87 (1974); T. Elsaesser, A. Seilmeir, W. Kaiser, *Opt. Commun.*, 44, 293 (1983).

3. S.A. Jamison, A.V. Nurmikko, and H.J. Gerritsen, *Appl. Phys. Letts.*, **29**, 640 (1976).

4. A.J. Alcock and P.B. Corkum, *Can. J. Phys.*, **57**, 1280 (1979).

5. P.B. Corkum, *IEEE J. Quant. Electron.*, **QE-21**, 216 (1985).

6. I. Ben-Zvi, *Advanced Accelerator Concepts, AIP Conference Proceedings* **279**, 590 (1993).

7. A. Fisher, J. Gallardo, J. Sandweiss, A. van Steenbergen, *Advanced Accelerator Concepts, AIP Conference Proceedings* **279**, 299 (1993).

8. W.D. Kimura, L. Steinhauer, G.H. Kim, S.C. Tidwell, I. Pogorelsky, K.P. Kusche, *Proceedings of the Particle Accelerators Conference*, Washington, D.C., May 17-21 (1993)

9. R.B. Palmer, *Particle Accelerators*, **11**, 81 (1980); W. Chen, et al, *Brookhaven National Laboratory Report*, BNL-43465 (1989).

10. A.F. Gibson, C.A. Rosito, C.A. Raffo, and M.J. Kimmit, *Appl. Phys. Letts.*, **21**, 356 (1972).

11. V.T. Platonenko and V.D. Taranukhin, *Sov. J. Quantum Electron.*, **13**, 1459 (1983).

12. T. Tajima and J.M. Dawson, *Phys.Rev.Lett.*, **43**, 267 (1979); A.M. Sessler, *Am.J.Phys*, **54**, 505 (1986);L.M. Gorbunov and V.I. Kirsanov, *Sov.Phys.JETP*, **66**, 290 (1987); P. Sprangle, E. Esarey, A. Ting, and G. Joyce, *Appl.Phys.Lett*, **53**, 2146 (1988).

13. J.R. Fontana and R.H. Pantell, *J.Appl.Phys.*, **54**, 4285 (1983);

14. S.C. Tidwell, G.H. Kim, and W.D. Kimura, *Appl.Opt.*, **32**, 5222 (1993).

15. R.D. Romea and W.D. Kimura, *Phys.Rev.*, **42D**, 1807 (1990).

16.J.R. Fontana, W.D. Kimura, L. Steinhauer, and I. Pogorelsky, *Proceedings of the Particle Accelerators Conference*, Washington, 2614 (1993).

FIGURE CAPTIONS

Fig.1. Picosecond pulse propagation in the CO_2 amplifier (initial intensity 1 MW/cm^2):
a) τ_0=3 ps pulse;
b) same after amplification with a total gain $g_0 l = 10$ in a regular 10-atm mixture;
c) same in a 5-atm isotopic mixture.
d) τ_0=30 ps pulse;
e) same after amplification with a total gain $g_0 l = 10$ in a 1-atm regular mixture;
f) same in a 10-atm regular mixture.

Fig.2. Picosecond pulse slicing set-up with a polarization rotation of the control beam.

Fig.3. 8-pass amplifier optical set up.

Fig.4. Experimental curves for energy evolution in 8-pass amplifier: (A) single-switched initial pulse; (B) τ_0=120 ps; (C) τ_0=60 ps.

Fig.5. Experimental autocorrelation curves measured after a 3-pass amplification of a single-switched CO_2 laser pulse (A) without a self-breakdown and (B) with a self-breakdown.

Fig.6. Arrangement for inverse Cherenkov interaction.

Fig.7. Schematic plan view of the ICA interaction gas cell.

Fig.8. Schematic optical layout of the radial polarization converter.

Fig.9. Combination of $sin^2\theta$ and $cos^2\theta$ beams yields radially polarized beam

Fig.10. Electron spectra measured after the ICA cell:
(a) laser off, mean e-beam energy 40 MeV;
(b) 0.7-GW laser on, hydrogen gas pressure 2.2 atm.

Fig.11. Two-stage multi-isotope amplifier system.

DISCLAIMER

This report was prepared as an account of work sponsored by an agency of the United States Government. Neither the United States Government nor any agency thereof, nor any of their employees, makes any warranty, express or implied, or assumes any legal liability or responsibility for the accuracy, completeness, or usefulness of any information, apparatus, product, or process disclosed, or represents that its use would not infringe privately owned rights. Reference herein to any specific commercial product, process, or service by trade name, trademark, manufacturer, or otherwise does not necessarily constitute or imply its endorsement, recommendation, or favoring by the United States Government or any agency thereof. The views and opinions of authors expressed herein do not necessarily state or reflect those of the United States Government or any agency thereof.

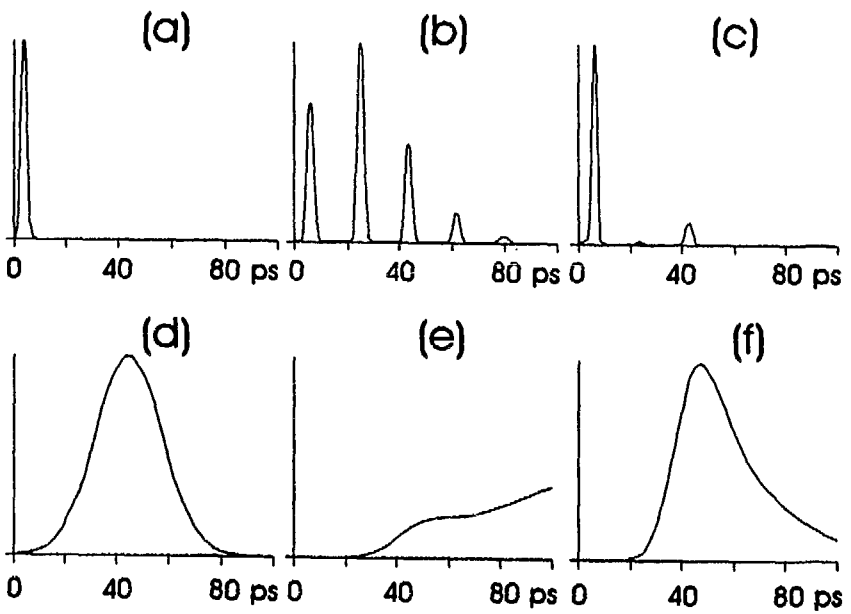

Fig.1

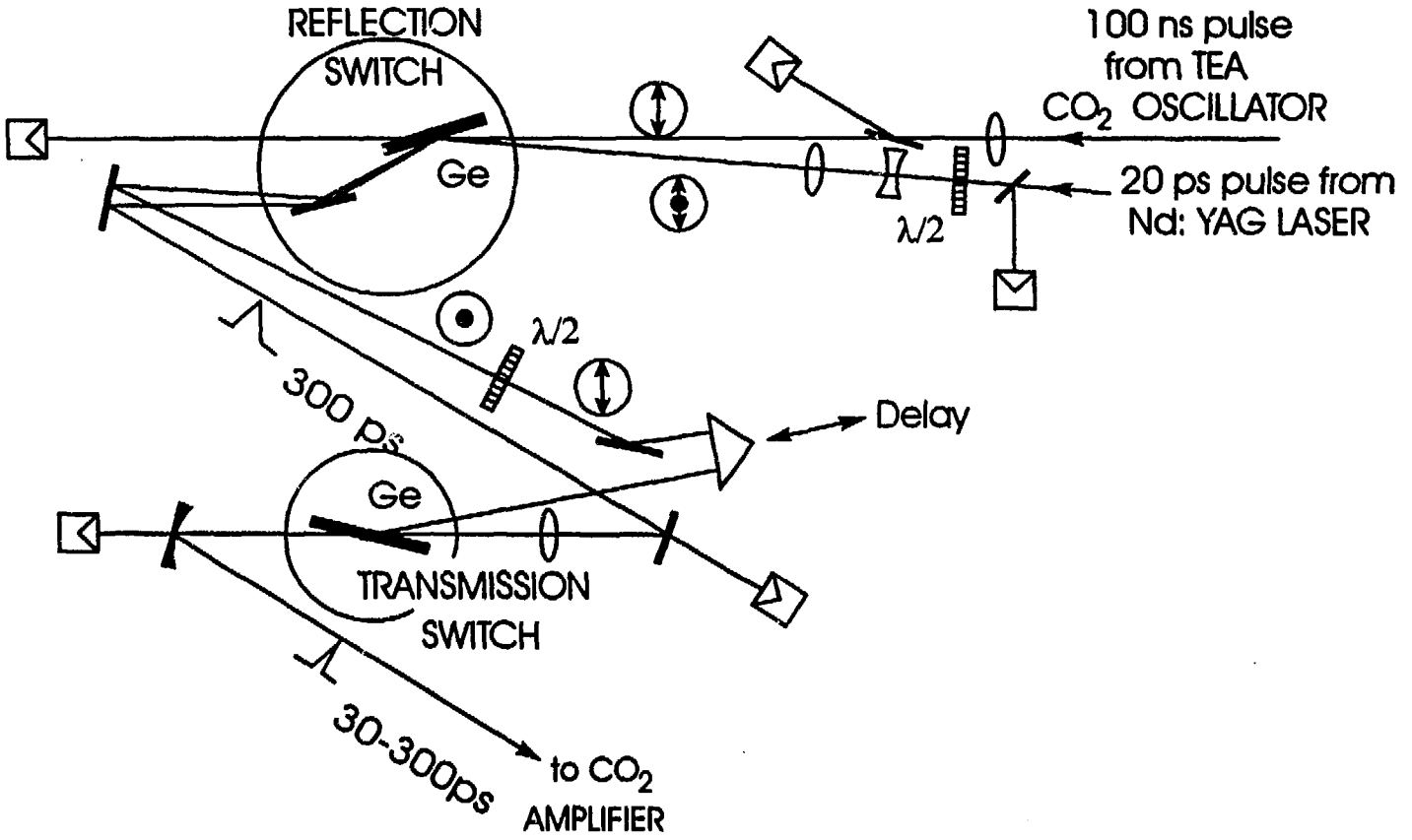
REFLECTION
SWITCH
Ge
100 ns pulse
from TEA
CO_2 OSCILLATOR
20 ps pulse from
Nd: YAG LASER
λ/2
λ/2
300 ps
Delay
Ge
TRANSMISSION
SWITCH
30-300ps
to CO_2
AMPLIFIER

Fig.2

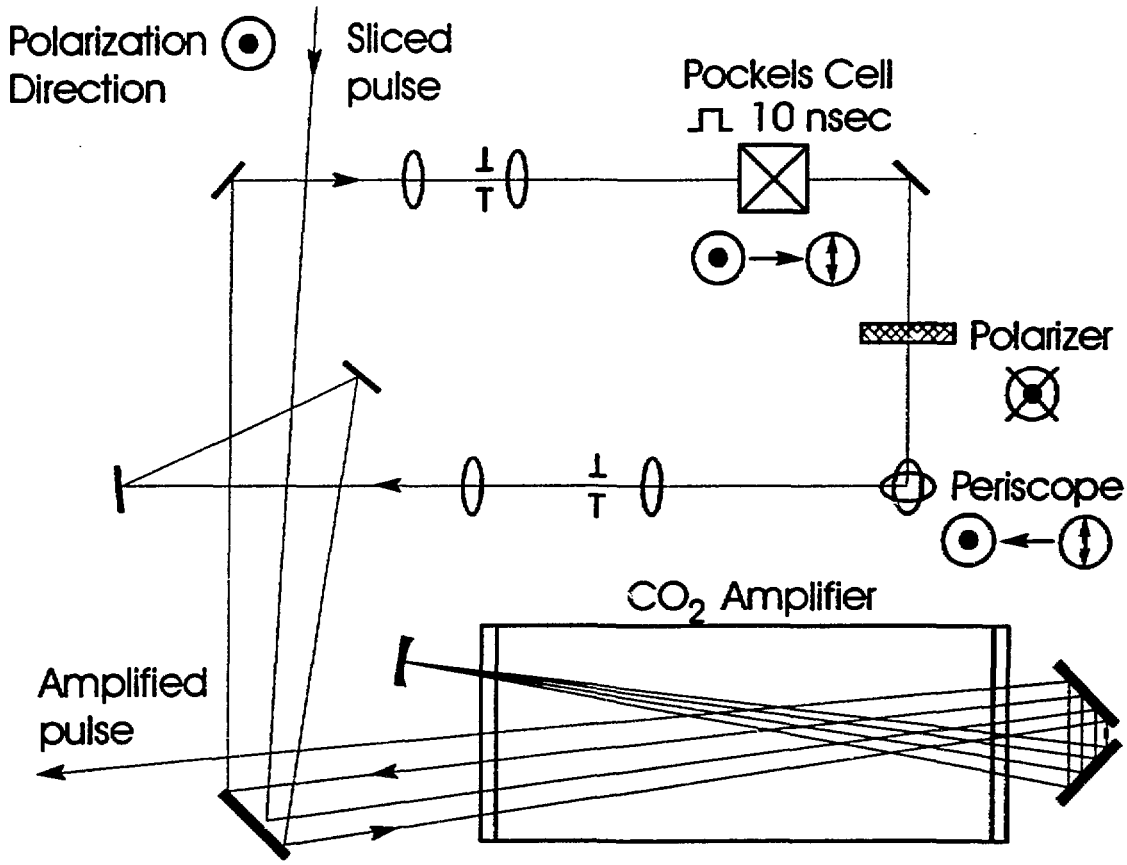
Polarization Direction
Sliced pulse
Pockels Cell
10 nsec
1/T
Polarizer
Periscope
1/T
CO_2 Amplifier
Amplified pulse

Fig.3

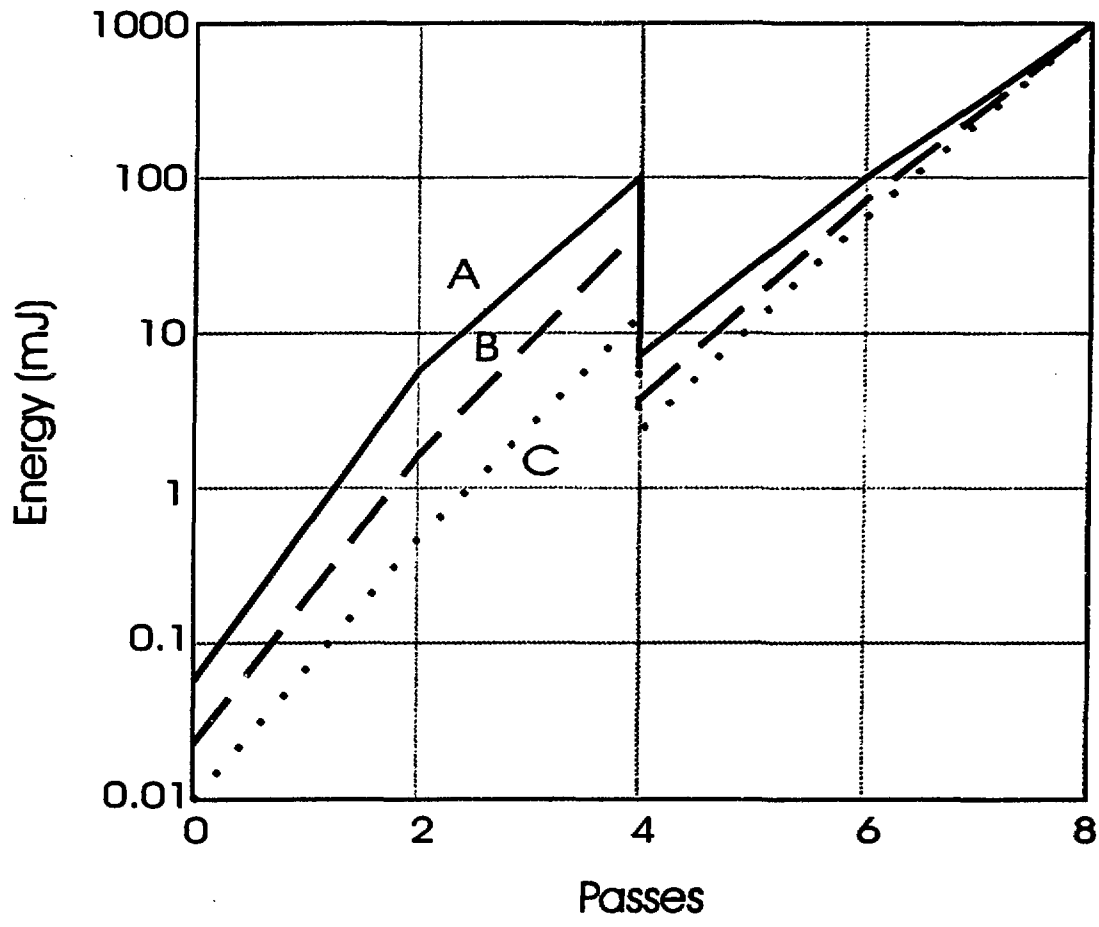

Fig.4

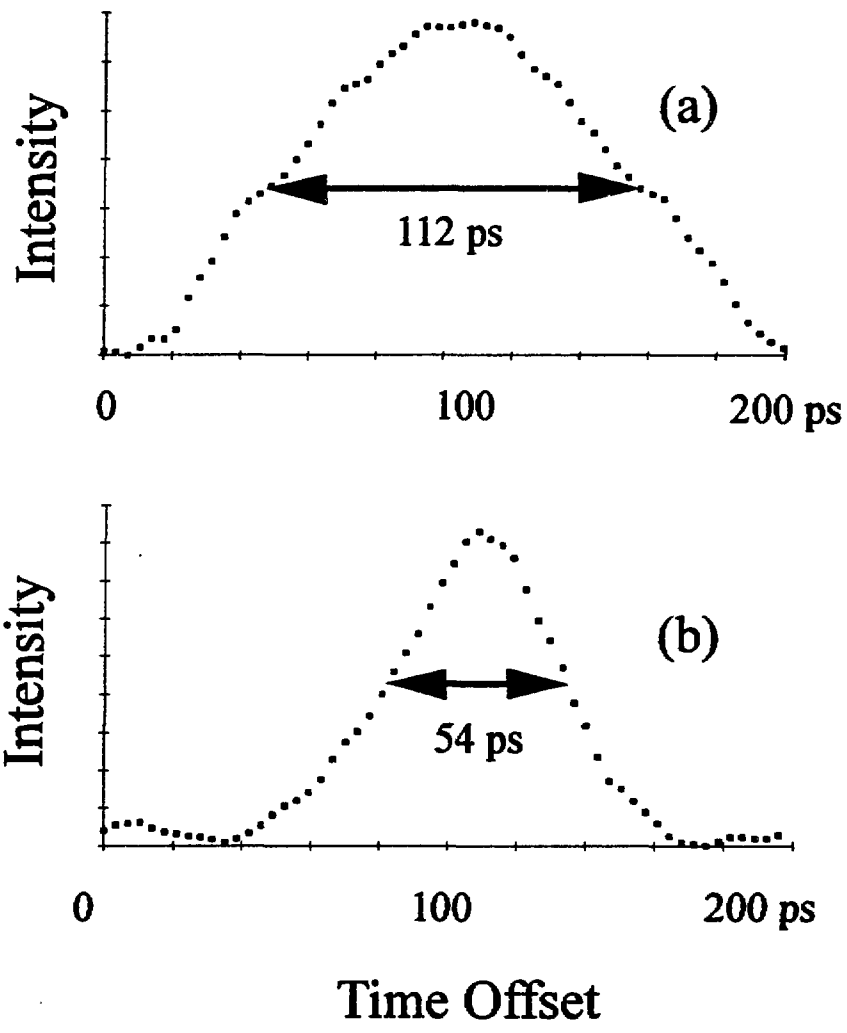
Intensity
(a)
112 ps
0
100
200 ps
Intensity
(b)
54 ps
0
100
200 ps
Time Offset

Fig.5

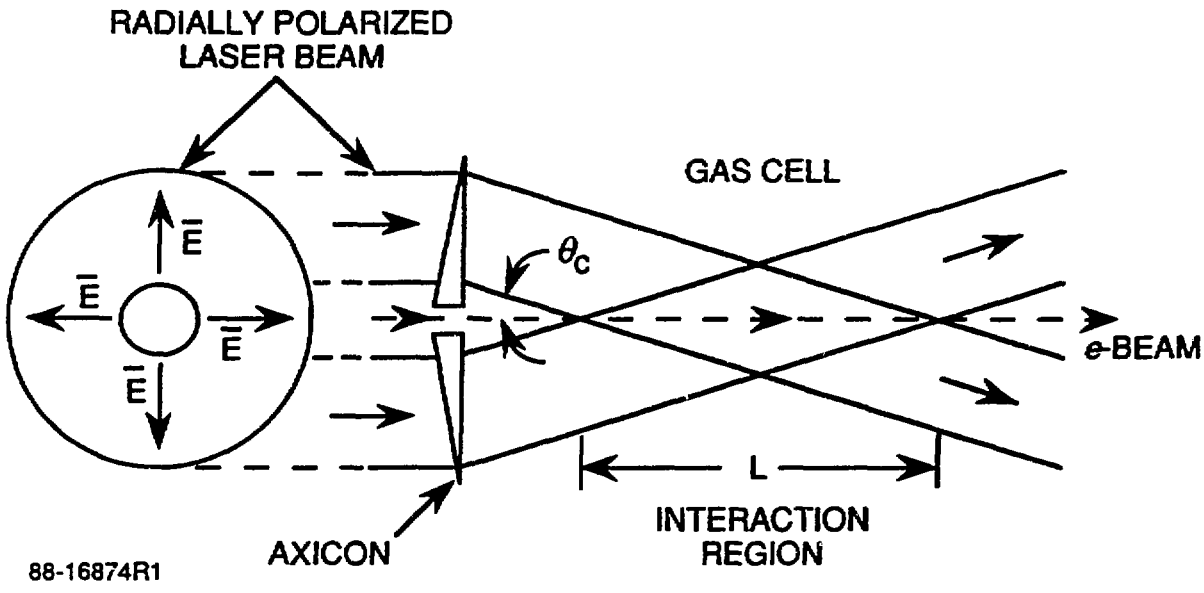
RADIALLY POLARIZED
LASER BEAM
GAS CELL
$\bar{E}$
$\bar{E}$
$\bar{E}$
$\bar{E}$
θ_c
e-BEAM
L
INTERACTION
REGION
AXICON
88-16874R1

Fig.6

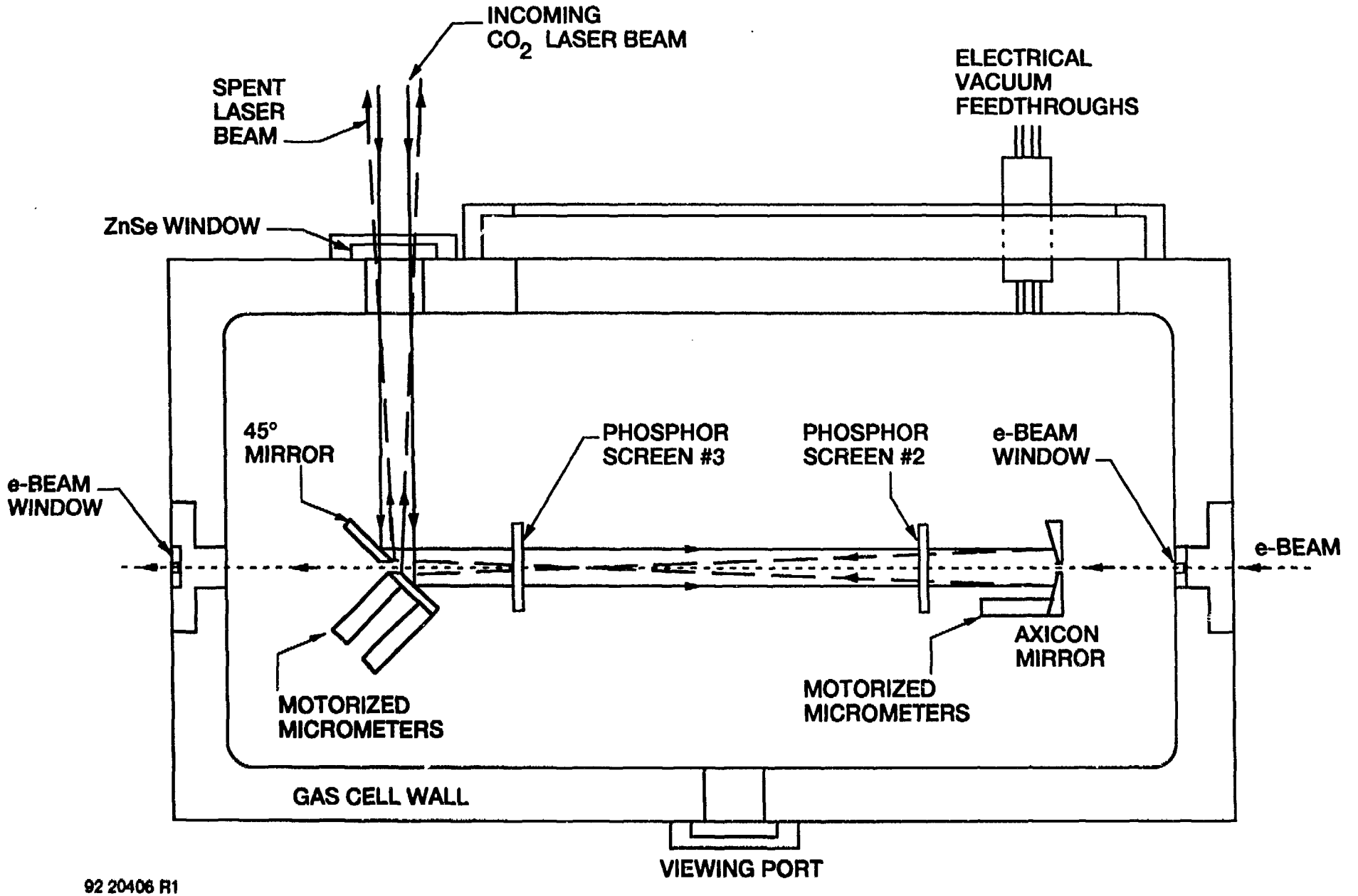
INCOMING
CO_2 LASER BEAM
SPENT
LASER
BEAM
ELECTRICAL
VACUUM
FEEDTHROUGHS
ZnSe WINDOW
45°
MIRROR
PHOSPHOR
SCREEN #3
PHOSPHOR
SCREEN #2
e-BEAM
WINDOW
e-BEAM
WINDOW
e-BEAM
AXICON
MIRROR
MOTORIZED
MICROMETERS
MOTORIZED
MICROMETERS
GAS CELL WALL
VIEWING PORT
92 20406 R1

Fig.7

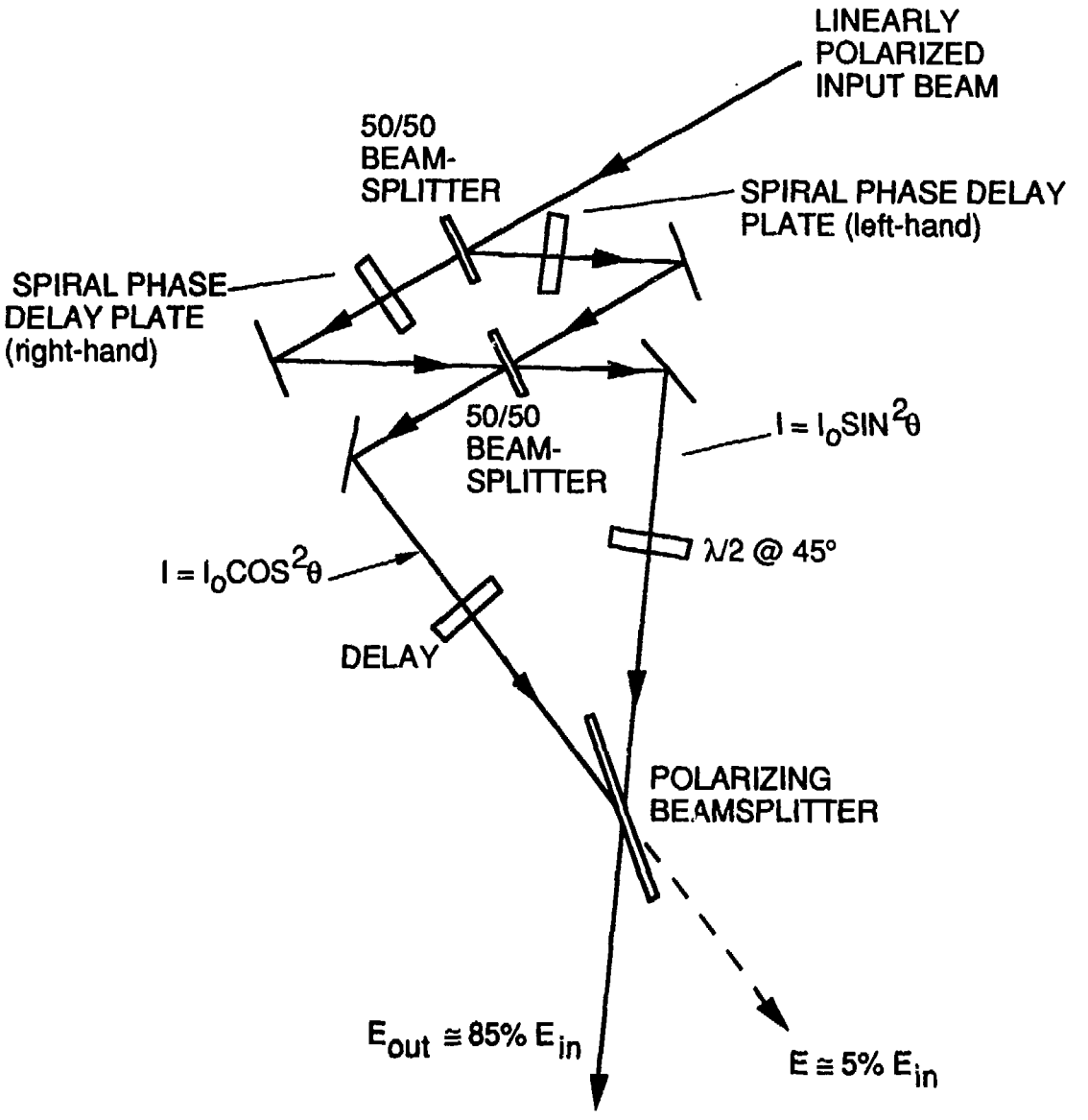
LINEARLY
POLARIZED
INPUT BEAM
50/50
BEAM-
SPLITTER
SPIRAL PHASE DELAY
PLATE (left-hand)
SPIRAL PHASE
DELAY PLATE
(right-hand)
50/50
BEAM-
SPLITTER
I = I0SIN2θ
λ/2 @ 45°
I = I0COS2θ
DELAY
POLARIZING
BEAMSPLITTER
Eout ≅ 85% Ein
E ≅ 5% Ein
89 18249 R3

Fig.8

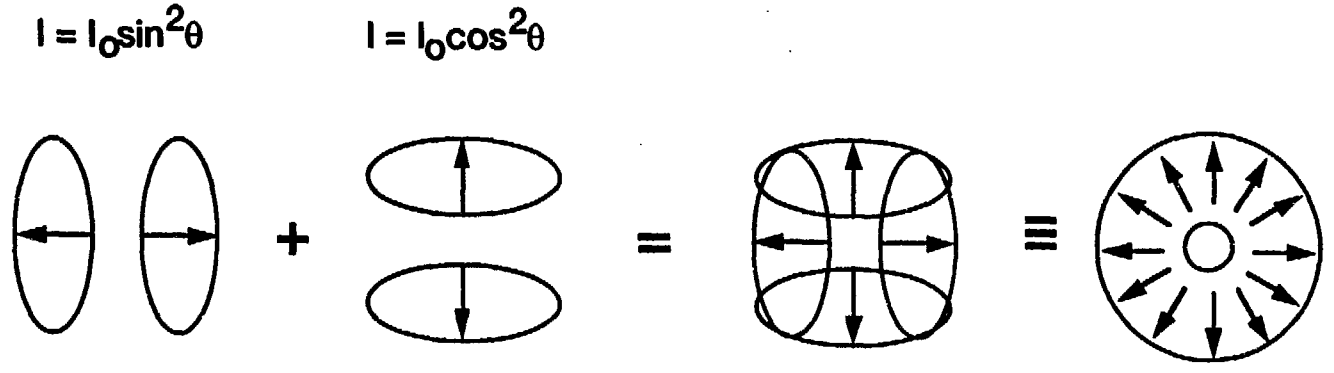

90 19228

Fig.9

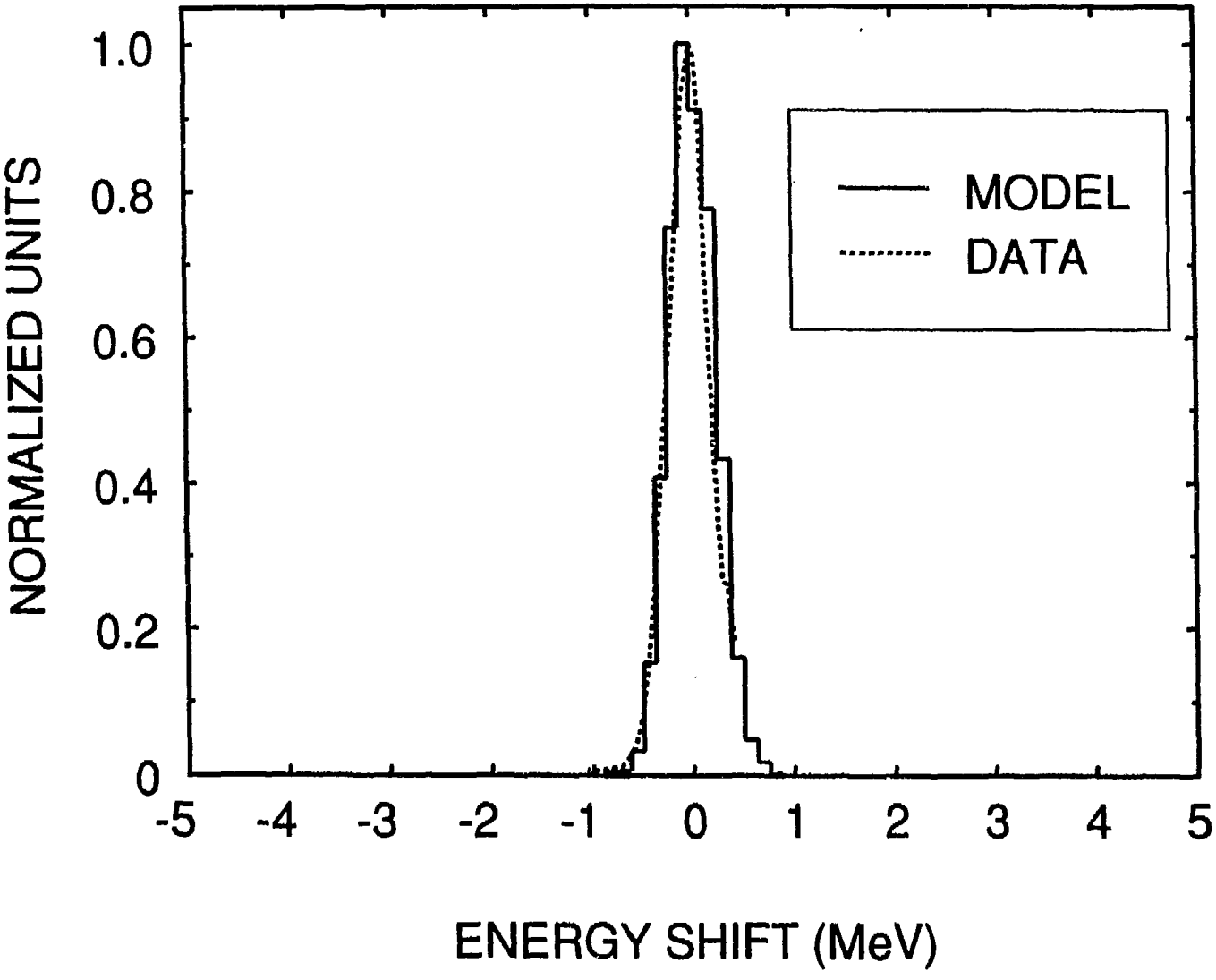
NORMALIZED UNITS
1.0
0.8
0.6
0.4
0.2
0
-5
-4
-3
-2
-1
0
1
2
3
4
5
ENERGY SHIFT (MeV)
MODEL
DATA

Fig.10(a)

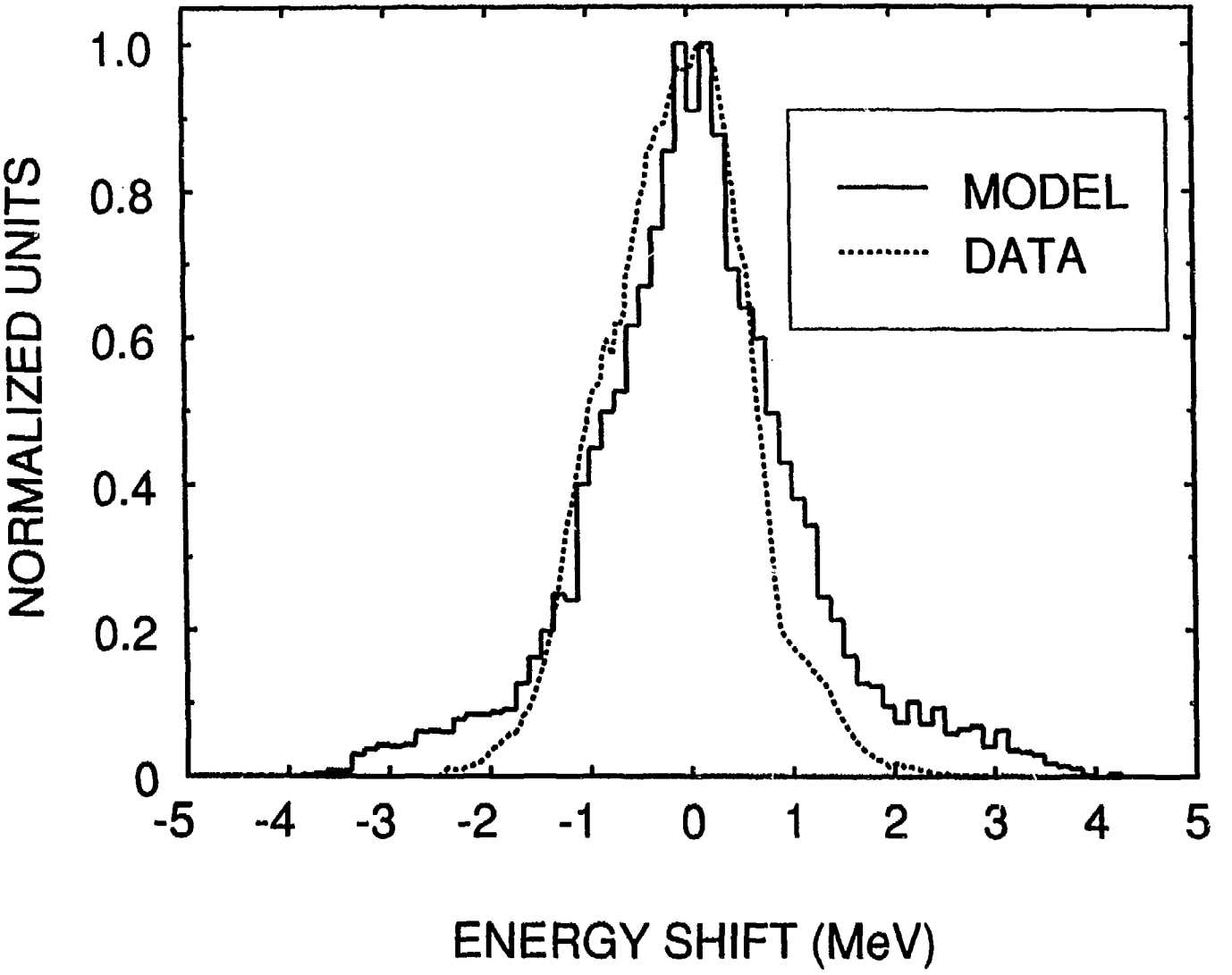
NORMALIZED UNITS
1.0
0.8
0.6
0.4
0.2
0
-5
-4
-3
-2
-1
0
1
2
3
4
5
ENERGY SHIFT (MeV)
MODEL
DATA

Fig.10(b)

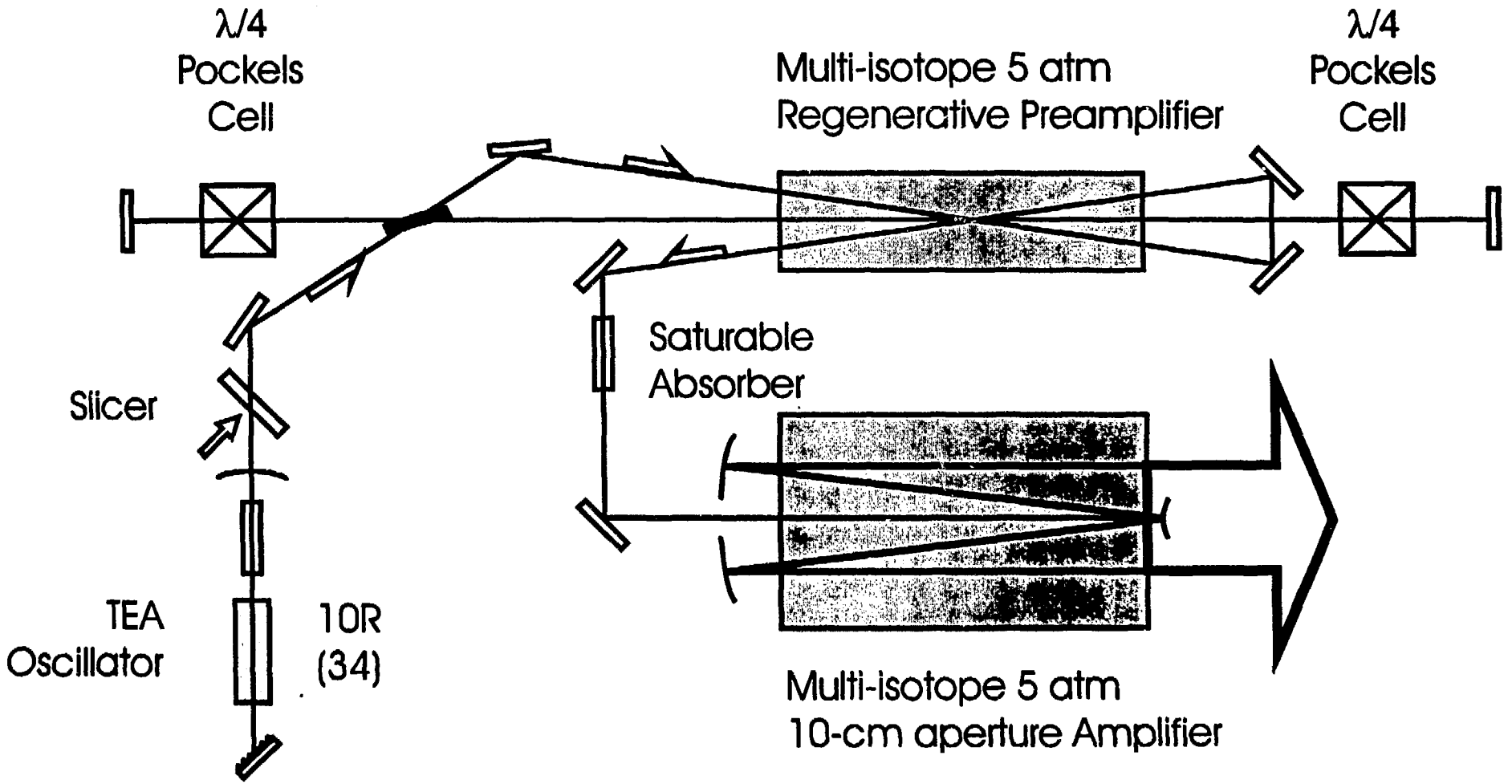
λ/4
Pockels
Cell
Multi-isotope 5 atm
Regenerative Preamplifier
λ/4
Pockels
Cell
Saturable
Absorber
Slicer
TEA
Oscillator
10R
(34)
Multi-isotope 5 atm
10-cm aperture Amplifier

Fig.11